Topological nodal line and superconductivity of highly thermally stable two-dimensional TiB_4

Lei Wang,[1,2] Mingfeng Liu,[1,2] Jiangxu Li,[1,2] Ronghan Li,[1] Hui Ma,[1] and Xing-Qiu Chen[1,2,*]

[1]*Shenyang National Laboratory for Materials Science, Institute of Metal Research, Chinese Academy of Sciences, 110016 Shenyang, People's Republic of China*

[2]*School of Materials Science and Engineering, University of Science and Technology of China, 110016 Shenyang, People's Republic of China*

(Received 30 August 2021; accepted 1 November 2021; published 12 November 2021)

By means of first-principles calculations, we study the electronic structures, lattice dynamics, electron-phonon coupling (EPC), and superconductivity of TiB_4 monolayer (TBML) and TiB_4 bilayer (TBBL). We find that both TBML and TBBL are nodal line semimetals, and the occurrences of their nodal lines are mainly due to the band inversions between B-$p_x + p_y$ and B-p_z for TBML and between Ti-$d_{xz} + d_{yz}$ and Ti-d_{z^2} for TBBL. The distortion of Ti atoms in the TBBL induces a horizontal glide mirror plane, which protects its nodal line against the spin-orbit coupling. The computed EPC constant λ of TBML is 0.65, higher than that of the TBBL with $\lambda = 0.35$. Both TBML and TBBL are identified to be phonon-mediated two-dimensional (2D) superconductors with the calculated $T_c = 1.66$ K and 0.82 K, respectively. The T_c of the TBBL can be further enhanced to 6.43 K by applying a tensile strain of 11%. Moreover, they exhibit excellent thermal stability. The coexistence of the topological nodal-line states around the Fermi level and superconductivity in the square-lattice TiB_4 monolayer may show more potential for realization of exotic physics.

DOI: 10.1103/PhysRevB.104.195123

I. INTRODUCTION

Superconductors with nontrivial electronic band structure have attracted plenty of attention due to the possibility of realizing novel quantum states, such as topological superconductors and Majorana fermions [1–3]. Nontrivial electronic band structure emerges in topological electronic materials, such as topological insulators and topological semimetals [4–7]. The topological insulator exhibits an insulating bandgap at its bulk phase and topologically protected nontrivial metallic helical states with a linear Dirac cone dispersion at its surface. Unlike topological insulators, topological semimetals display the topologically protected nontrivial surface states and topologically nontrivial Dirac or Weyl cone dispersions at their bulk state. The appearance of the Dirac or Weyl cones around the Fermi level at the bulk phases of topological semimetals makes them not easy to achieve topological nontrivial states and superconductivity simultaneously. The reason is that the carrier density of topological semimetal near Fermi level normally is low due to the existence of Dirac point, Weyl point, or nodal line. Yet, for a superconductor, a higher carrier density near the Fermi level is beneficial to achieve a higher critical temperature [8]. Therefore, exploring the superconductivity in topological semimetals is crucial for the study of topological superconductivity.

Metallic borides (MBs) are an important class of inorganic solid with a large variety of crystal structures, originated from the ability to form multicentred boron bonds to overcome electron deficiency [9,10]. Based on this, zero-dimensional (0D) boron centers, one-dimensional (1D) boron chains [11], two-dimensional (2D) boron layer [12], and three-dimensional (3D) boron network [13] are achieved in MBs, which makes MBs have various properties, such as superhardness material [14–16], topological semimetals [17,18], and superconductors [12,20,21].

The well-known superconductor in 3D MBs is MgB_2, discovered to be superconductive at a remarkably high critical temperature $T_c = 39$ K [12,19,20]. Such a high T_c of MgB_2 originates from the fact that its interband anisotropy enhances the effective EPC constant relevant to superconductivity [21]. Interestingly, ZrB_2 and TiB_2 crystallize in the same lattice structure as that of MgB_2, and both of them exhibit topological Dirac nodal-net fermions [17,18]. However, none of them is a superconductor [22].

The situation becomes a bit different in their 2D MBs. Several 2D MBs nodal line semimetals (NLSs) are theoretically reported as superconductors. Using high-throughput structural searching, a 2D AlB_6 material is identified as a nodal-line material and predicted as superconductor with $T_c = 4.7$ K [23]. Surprisingly, the T_c of AlB_6 monolayer can be greatly enhanced up to 30 K by applying a tensile strain of 12%. Furthermore, even though hydrogen adatoms destroy the Dirac state of monolayer TiB_2, monolayer TiB_2H is predicted as a phonon-mediated superconductor with T_c of 8 K [24]. This predicted T_c also increases with the applications of external tensile strains.

To date, 2D coexisted topological nontrivial and superconducting materials have caught plenty of attention, e.g., NLSs AlB_6 [23], 2D W_2N_3 [25], type-II Weyl semimetal WTe_2 [26,27], one-unit-cell FeSe [28], and NLSs Cu_2Si [29]. However, besides the NLSs Cu_2Si [29], rare veritable

*xingqiu.chen@imr.ac.cn

one-atomic-thickness 2D materials were reported. Thus, the problem remains open as to whether the superconductivity and topological nodal-line states would occur simultaneously in one-atomic-thickness MBs.

To answer this question, we focus on one-atomic-thickness monolayer TiB_4 (TBML) and bilayer TiB_4 (TBBL). Both TBML and TBBL are stable theoretically [30,31]. TiB_4 is a candidate material for energy storage of H_2 and CH_4 [32] and Li-ion batteries anodes [30]. By employing first-principles calculations, we derived their electronic structures, lattice dynamics, EPC constant, and phonon-mediated superconductivity. The results reveal that both TBML and TBBL are nodal-line semimetals and their EPC constants are as high as 0.65 and 0.35, respectively. The softening ZA (out-of-plane acoustic) mode in the TBML is mainly responsible for its higher EPC constant. Both TBML and TBBL are phonon-mediated 2D superconductors with the predicted transition temperature of $T_c = 1.66$ K and 0.82 K, respectively. The TBBL is dynamically stable under the biaxial tensile strain ranging from 1%–11%. The predicted T_c of the TBBL increases to 6.43 K with a tensile strain of 11%. Both TBML and TBBL show excellent thermal stability, which will facilitate their experimental synthesis.

II. COMPUTATIONAL METHODS

First-principles calculations were performed by using the Vienna *ab initio* simulation package (VASP) [33–35]. The exchange-correlation potential was treated by the generalized gradient approximation (GGA) of the Perdew-Burke-Ernzerhof (PBE) type [36]. The cutoff energy for plane-wave expansion was 500 eV and the k-point sampling grid in the self-consistent process was $15 \times 15 \times 1$. The crystal structure was fully relaxed until the residual forces on each atom became less than 0.001 eV/Å and the energy precision became less than 10^{-6} eV. A vacuum of 20 Å between layers was used to model monolayer and bilayer TiB_4.

The calculations (EPC and superconductivity) were performed with local density approximation [37] as implemented in the Quantum-ESPRESSO [38,39] package with ultrasoft pseudopotentials (USPP) found in the standard solid-state pseudopotentials (SSSP) library. The kinetic energy cutoff and the charge density cutoff of the plane wave basis were chosen to be 100 and 800 Ry for TBML and 80 and 640 Ry for TBBL, respectively. All the structures were relaxed to their equilibrium positions such that the forces acting on each atom became smaller than 10^{-6} Ry/Bohr. We used Marzari-Vanderbilt cold smearing [40] of 0.02 Ry to speed up the convergence. The self-consistent electron density was evaluated by employing $36 \times 36 \times 1\,\vec{k}$ mesh for TBML and $24 \times 24 \times 1\,\vec{k}$ mesh for TBBL. The EPC and superconductivity are calculated using the density functional perturbation theory (DFPT) [41]. Both phonon and EPC were calculated using a $6 \times 6 \times 1\,\vec{q}$ mesh for both the TBML and TBBL.

The Wannier-based Hamiltonian was constructed by the Wannier90 package [42]. Berry phase and edge-state calculations based on maximally-localised Wannier functions were done using the WannierTools package [43].

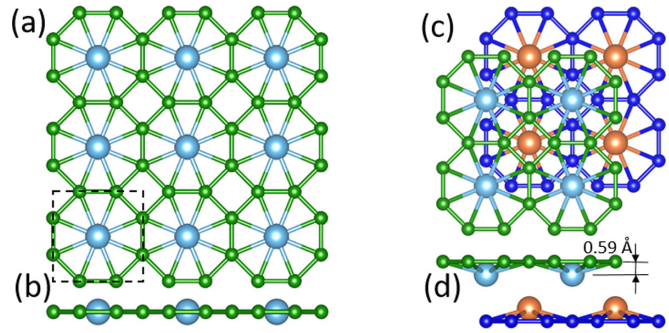

FIG. 1. The crystal structure of 2D TiB_4. (a) The top and (b) the side view of the optimized TBML. The cyan atoms denote Ti atoms and the green atoms denote B atoms. (c) The top and (d) the side view of the optimized TBBL. The cyan and orange atoms denote Ti atoms of upper and bottom layer, respectively. The green and blue atoms denote B atoms of the upper and bottom layers, respectively.

III. RESULTS AND DISCUSSIONS

A. Structural models of TBML and TBBL

The TBML, shown in Figs. 1(a) and 1(b), exhibits a planar edge-sharing $Ti©B_8$ wheel structure with space group P4/mmm, and the optimized lattice constants of $a = b = 4.106$ Å. The optimized Ti-B bond length is 2.218 Å. The B-B bond length in the boron squares is 1.716 Å, whereas the B-B bond length in the sharing edges is 1.679 Å. These results are in good agreement with the reported data in the previous papers [30,32].

Interestingly, when it comes to the double-layer stackings of the TBML, here named as TiB_4 bilayer (TBBL), the structures are changed. After optimizing several different TBBLs, the most energetically favorable configuration displayed in Figs. 1(c) and 1(d), is the one that upper-layer Ti atoms locate above the center of the B square rings in the sublayer and vice versa. On closer inspection, we found that the Ti atoms no longer keep in the horizontal plane with B atoms, but move toward another layer by 0.593 Å, leading to the space group changing from P4/mmm (No. 136) to P4/nmm (No. 129). The optimized lattice constants of TiB_4 bilayer is $a = b = 4.075$ Å. They are a little bit smaller than those of the TBML ($a = b = 4.106$ Å). Moreover, the vertical interlayer distance between the B-B layers is 2.822 Å, and the calculated interlayer interaction energy is 280 meV per atom. These results are consistent with the previously reported values [30,32]. Such a change of stacking and the structure of the TBML will promote different electronic properties in the TBBL.

B. The electronic properties of the TBML and the TBBL

The electronic band structures of the TBML without the inclusion of spin-orbit coupling (SOC) are shown in Figs. 2(a) and 2(b). We find that, in Fig. 2(a), there is one band degenerate node at the high symmetry point M near the Fermi level. We doubly checked the bandgap at this degenerate node, and it is a zero-gaped parabolic-like node point (PNP1), as shown in Fig. 2(c). The other zero-gaped parabolic-like degenerate node point (PNP2) in Fig. 2(d) is also observed at the high-symmetry point Γ about 0.25 eV above the Fermi level.

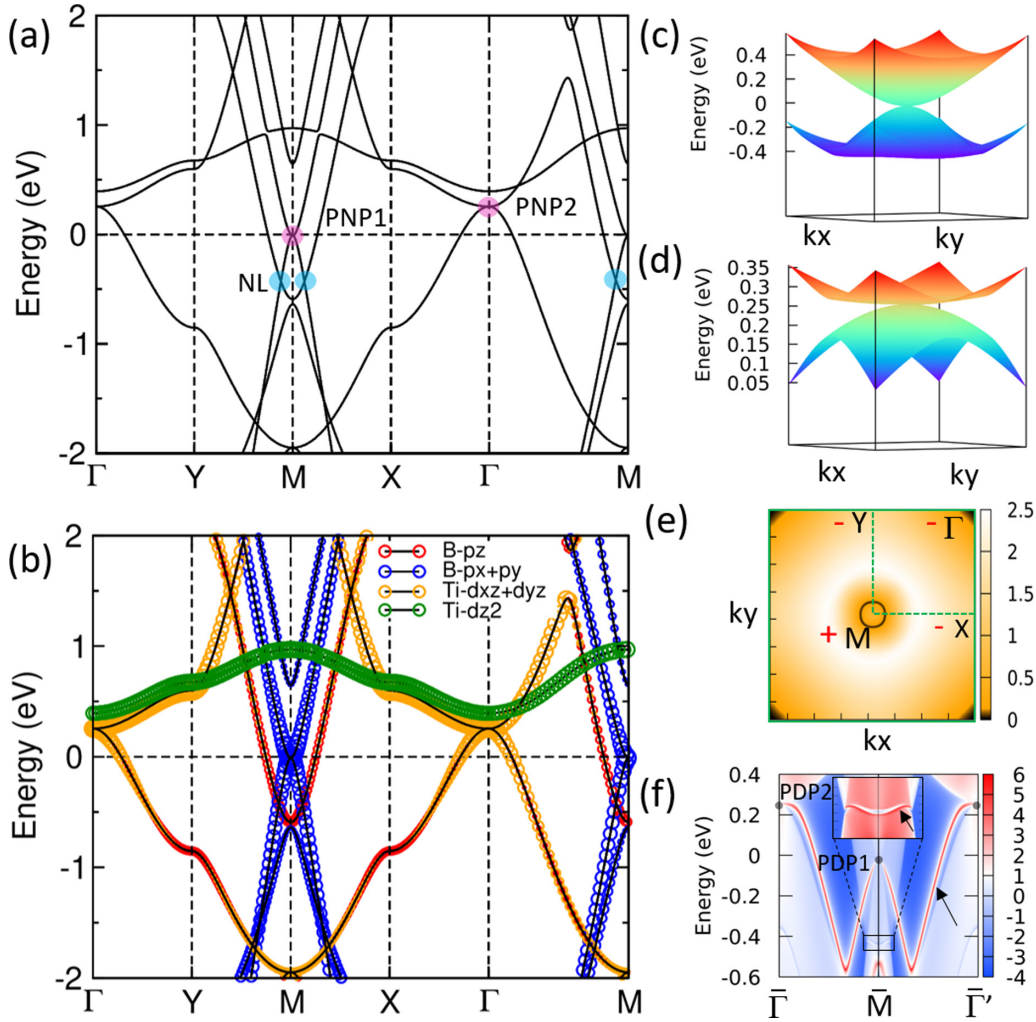

FIG. 2. The electronic structures of the TBML. (a) The band structure and (b) the orbital-resolved band structure of the TBML, where the red and the blue circles represent the projections of the B p_z and $p_x + p_y$ orbits, respectively. (c) and (d) are the 3D band dispersion around the PNP1 and PNP2, respectively. (e) The gap between $N_{\rm occ}$ band and $N_{\rm occ}$+1 bands in the whole BZ. The black circle around M is the nodal line shown in (a). The red + and – are the mirror eigenvalues of time-reversal invariant points. (f) The projected edge band spectrum of the (010) edge of the TBML.

To further understand whether these two PNP1 and PNP2 are topologically nontrivial, the Wannier-based Hamiltonian is obtained by combining first-principles calculations and maximally-localised Wannier functions calculations. Then, the Berry phases of these two PNPs are derived as [43,44]

$$\gamma_n = \oint_C A_n \cdot d\boldsymbol{k}, \tag{1}$$

where $A_n = i\langle u_{n,\mathbf{k}} \mid \nabla_{\mathbf{k}} u_{n,\mathbf{k}}\rangle$ is the Berry connection and $u_{n,\mathbf{k}}$ is the lattice periodic part of the Blöch wave functions. The results show that these two PNPs host the zero Berry phases, indicating their topologically trivial nature.

We still observe that, in Fig. 2(a), there are three band crossing nodes around –0.4 eV at the high-symmetry lines of Γ-X, Γ-Y, and Γ-M below the Fermi level, respectively. In order to identify whether or not these three band crossing nodes are connected to each other, we have drawn the $N_{\rm occ}$ and $N_{\rm occ}$+1 bands in the whole BZ, where the $N_{\rm occ}$ is the total number of the occupied states of the TBML. As displayed in Fig. 2(e), there is one black ring around the centered M point formed by the contact between $N_{\rm occ}$ and $N_{\rm occ}$+1 bands. This fact means the three nodes near the M point in Fig. 2(a) sit at such a nodal ring. The orbital-resolved band structure [Fig. 2(b)] displays that the nodal ring is caused by the inversion between the p_z and $p_x + p_y$ orbits of the boron atoms, indicating that the TBML is a NLS. Moreover, since the Z_2 number [45] based on the Berry phase for the 3D NLSs does not work in the 2D case, we then calculated the Z_2 number of the TBML by the method proposed in Ref. [46], where the Z_2 number of 2D materials can be defined as $Z_2 = \xi_\Gamma \xi_X \xi_Y \xi_M = (-1)^N$. Here, N is the total number of nodal rings and the $\xi_a = \prod_{n=1}^{N_{\rm occ}} \xi_{\rm an}$ [$\xi_{\rm an}$ is the mirror eigenvalue (+1 or –1) for each state at any k points]. In a 2D spinless system with the time-reversal symmetry, Γ(0, 0), X(0.5, 0), Y(0, 0.5), and M(0.5, 0.5) are the four time-reversal invariant points. Figure 2(e) shows the ξ_{an} at Γ, X, Y, and M by – and +. There are one + and three –, namely $Z_2 = (+1)^1(-1)^3 = (-1)^1$, in accordance with the fact that there is a topological nontrivial nodal ring surrounding the M point in the BZ of the

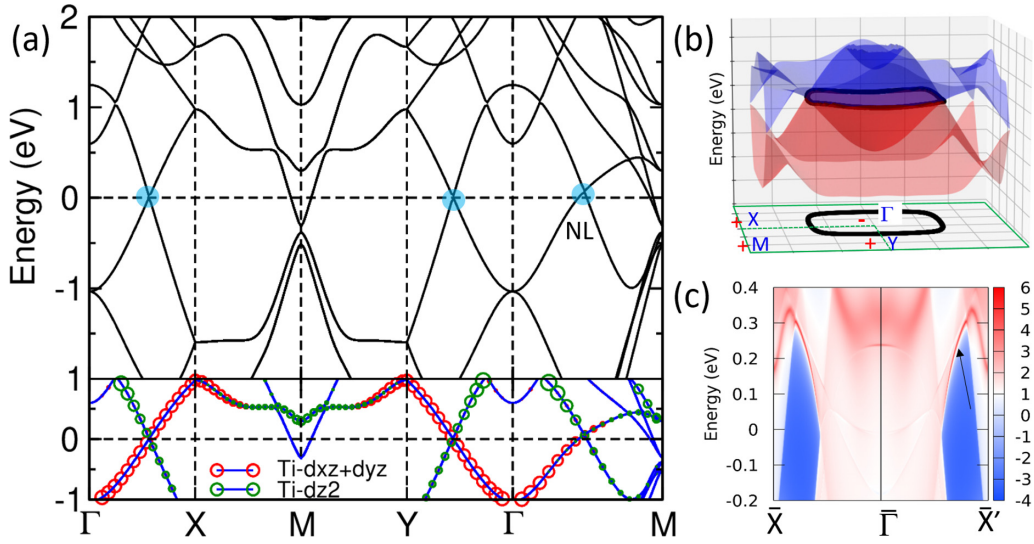

FIG. 3. The electronic structures of the TBBL. (a) The band structure and the orbital-resolved band structure of the TBBL. (b) The 3D band of $N_{\rm occ}$ (red) and $N_{\rm occ}+1$ (blue) band in the whole BZ. The black 3D-snake-like ring is the nodal ring of the TBBL. The black ring at the bottom is the projection of the nodal ring. The red + and – are the mirror eigenvalues of time-reversal invariant points. (c) The projected edge band spectrum of the (010) edge of the TBBL.

TBML. We have compiled the topologically projected edge electronic band at the (010) edge of the TBML. As shown in Fig. 2(f), there is an apparent edge state that appears inside the projection of the nodal loop, which supports the results of the Z_2 calculation and confirms the topological properties of the TBML.

We further analyzed the electronic band structure of the TBBL TiB_4 in Figs. 3(a) and 3(b), exhibiting a quite different electronic structure from that of its monolayer. As shown in Fig. 3(a), there are three nearly linear crossing points near the Fermi level along the high-symmetry lines of Γ-X, Γ-Y, and Γ-M, respectively. The orbital-resolved band structure shows that all of them are caused by the band inversion between the $d_{xz}+d_{yz}$ and d_{z^2}-like states of Ti atoms, as shown in the low panel in Fig. 3(a). This is apparently different from the band inversion in the TBML. In order to identify whether or not these three points are connected to each other, we also drew the $N_{\rm occ}$ and $N_{\rm occ}+1$ bands in the whole BZ. As displayed in Fig. 3(b), all of these three crossing points come from a Γ-centered energy-waved rectangle-shape-like nodal ring formed by the contact between red ($N_{\rm occ}$ band) and blue ($N_{\rm occ}+1$ band) hook faces, with the projection of a rectangle nodal line, as shown in the bottom of Fig. 3(b). In similarity, we have calculated the mirror eigenvalues (+ or –) at the four time-reversal invariant points Γ, X, Y, and M, $Z_2 = \xi_\Gamma\xi_X\xi_Y\xi_M = (-1)^1(1)^3 = (-1)^1$. Thus, this result reveals there exists only one nodal line around the centered Γ point, and this nodal line is topologically nontrivial. Furthermore, we derived its topologically protected nontrivial edge states on its (010) edge boundary in Fig. 3(c). As expected, a bright nontrivial edge state appears, located outside the nodal ring. This is different from the nontrivial edge states of the nodal ring of the TBML, which sits inside the nodal ring. Note that, due to buckled TiB_4 monolayer, the TBBL holds a glide mirror plane between two buckled TBMLs. This feature makes its nodal line highly robust against the SOC [47].

C. Electron-phonon coupling and superconductivity

We derived the phonon dispersions, phonon DOS, Eliashberg function as well as accumulated EPC constant of the TBML, as shown in Fig. 4. The absence of any imaginary mode of the phonon spectra indicates that the TBML is dynamically stable. Its highest frequency of 1082 cm^{-1} is much higher than those of MoS_2 (473 cm^{-1}) [48] and Cu_2Si (421 cm^{-1}) [29], but smaller than those of graphene (1600 cm^{-1}) [49], χ_3-B (1290 cm^{-1}) [50], β_{12}-B (1200 cm^{-1}) [50], and B_2C (1243 cm^{-1}) [51]. The higher frequency indicates the strong bonding interactions between its component atoms. The mechanical representation, at the Γ point, is $M = A_{1g} + A_{2g} + 2A_{2u} + B_{1g} + B_{2g} + B_{2u} + 3E_u + E_g$, where the acoustic modes are A_{2u} and E_u, and the other modes belong to the optical ones. In detail, both A_{2u} and E_u are the IR active modes, and A_{1g}, B_{1g}, B_{1g}, and E_g are the Raman active

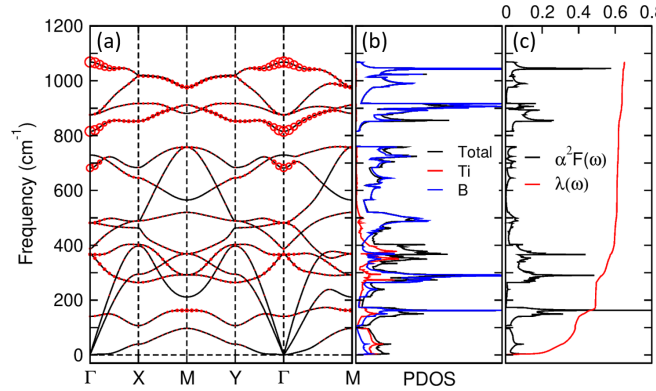

FIG. 4. (a) The phonon dispersion of the TBML, the area of the red circles represents the strength of phonon linewidth $\gamma_{q,\nu}$, (b) phonon DOS, and (c) Eliashberg function $\alpha^2F(\omega)$ with accumulated EPC constant $\lambda(\omega)$.

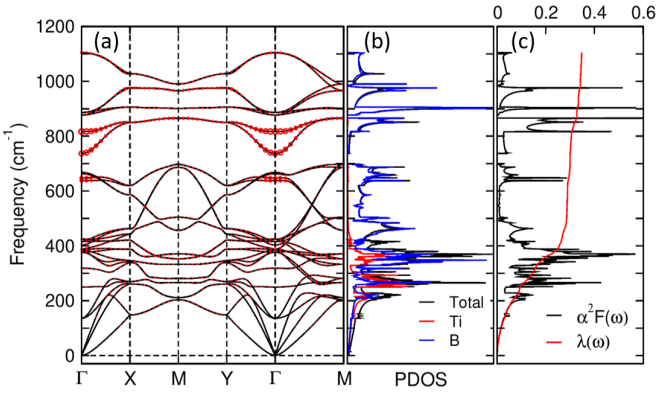

FIG. 5. (a) The phonon dispersion of the TBBL, the area of the red circles represents the strength of phonon linewidth $\gamma_{q,\nu}$, (b) phonon DOS, and (c) Eliashberg function $\alpha^2F(\omega)$ with accumulated EPC constant $\lambda(\omega)$.

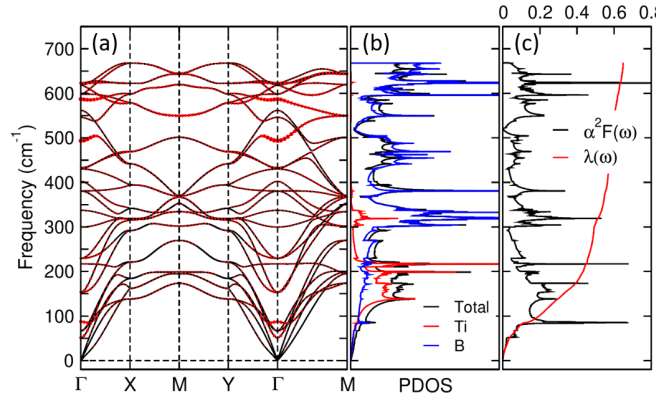

FIG. 6. (a) The phonon dispersion of the TBBL with a tensile strain 11%, the area of the red circles represents the strength of phonon linewidth $\gamma_{q,\nu}$, (b) phonon DOS, and (c) Eliashberg function $\alpha^2F(\omega)$ with accumulated EPC constant $\lambda(\omega)$.

modes. For the three acoustic modes, the in-plane longitudinal acoustic (LA) and in-plane transverse acoustic (TA) modes are almost linear. However, the out-of-plane acoustic (ZA) mode is soft and nearly quadratic, which reflects well the 2D nature of this monolayer. This feature is also observed in graphene [49], MoS_2 [48], and other 2D materials [52,53]. Interestingly, the lowest frequency optical (LFO) branch has the almost same tendency as the ZA mode does (We will discuss the effect of this mode on the EPC in the following text). For the partially decomposed phonon density of states [Fig. 4(b)], the low-frequency part of the phonon DOSs mainly come from the vibration of Ti atoms, whereas that of B atoms contribute mostly to the optical branches. Physically, this fact is mainly caused by the difference in their atomic masses.

Using the derived Eliashberg function $\alpha^2F(\omega)$, we analyzed the contribution of each phonon mode to the accumulated EPC constant of $\lambda(\omega)$. As shown in Fig. 4(c), the low-frequency part especially the ZA mode dominates the EPC constant. In detail, the ZA mode and the LFO branch contribute to the first and second peaks of the Eliashberg function with the EPC constant of 0.38 (58%) and 0.11 (17%), respectively, among the total EPC constant of 0.65. This is quite similar to Cu_2Si [29]. The phonon linewidth showed in Fig. 4(a) suggests, for the low-frequency part, these two Eliashberg function peaks mainly come from the vibration modes of the ZA and LFO branches from both Ti and B atoms at the M point, and for the high-frequency part, the Eliashberg function peaks mainly come from three optical modes (B_{1g}, B_{2g}, and A_{1g}) of the B atoms at the Γ point.

In order to investigate the thickness dependence of the EPC, we derived the phonon dispersions, phonon DOSs, Eliashberg function, and the accumulated EPC constant of the TBBL in Fig. 5. Note that no imaginary mode exists in its phonon dispersion, indicating its dynamical stability. As compared to the TBML, there are several differences in the TBBL: (i) the highest-frequency of the TBBL is 1187 cm^{-1}, which is higher than that of 1087 cm^{-1} in the TBML, suggestive of its stronger bonding interactions and (ii) In the region within the frequency lower than 500 cm^{-1}, as what the PDOSs display in Fig. 5(b), there are more phonon modes between 250 cm^{-1} and 500 cm^{-1} in comparison with the TBML. There is no apparent soft mode at frequencies less than 250 cm^{-1}. Physically, it is mainly since, when two TBML layers are stacked together, Ti atoms move toward another layer to cause the difference in their vibrational environment. The total EPC constant of the TBBL is 0.35, lower than that of TBML of 0.65. This kind of behavior that the EPC constant decreases with increasing the thickness is also in 2D materials of CoO_2 [56] and TaS_2 [57].

In terms of the derived Eliashberg function $\alpha^2F(\omega)$, we further calculated the logarithmic average phonon frequencies by $\omega_{\log} = \exp[\frac{2}{\lambda}\int_0^\infty \frac{d\omega}{\omega}\alpha^2F(\omega)\log\omega]$ and derived the superconductivity critical temperature using the simplified Allen-Dynes-modified McMillan formula [58], $T_c = \frac{\omega_{\log}}{1.2}\exp[\frac{-1.04(1+\lambda)}{\lambda-\mu^*(1+0.62\lambda)}]$. For the TBML, the $\omega_{\log}$ and T_c are 57.61 K and 1.66 K (2.50 K, $\mu^* = 0.05$), respectively. These values are lower than those of NLS Cu_2Si (83.59 K and 4.03 K, see Table I) and those of non-one-atomic-thickness 2D materials (e.g., the Ca-intercalated bilayer graphene C_6CaC_6 (4.0 K) [59,60], 2D tetr-Mo_2B_2 (344.84 K, 3.9 K) [55], 2D Dirac semimetals AlB_6 (4.7 K, $\mu^* = 0.05$) [23], and 2D MA_2Z_4 materials $TaSi_2N_4$ (9.7 K, $\mu^* = 0.1$) [61]. For the TBBL, the $\omega_{\log}$ and T_c are 459.12 K and 0.82 K, comparable to those of CaC_6 (309.9 K and 1.4 K) [62], but higher than those of tri-Mo_2B_2 (295.0 K, 0.2 K).

We note that in our above discussions, both the TBML and TBBL are freestanding. In reality, they grow on a substrate, leading to certain external strain to the samples. In fact, strain engineering is widely used to modulate the electronic properties, EPC constant, and superconductivity of 2D systems, such as graphene [63], AlB_6 [23], and other 2D materials [29,54,64]. However, as shown in Fig. 4(a), the ZA mode of the TBML is so soft that applying both tensile and compressive strains will make it much softer, and even negative. In this regard, the impact of strain on the TBML is not discussed here. Therefore, strain engineering is only used for TBBL to investigate its EPC constant and superconductivity, and the results show in Fig. 6. Firstly, we analyzed the effect of the biaxial strains on the TBBL. Figure 7 shows the calculated phonon spectra of TBBL with strains from –1% to 12%. Among them, there is no imaginary frequency in the whole

TABLE I. Summary of μ^*, $\omega_{\log}$ (in K), λ, and T_c (in K) for the 2D superconductors. The percentage in the bracket behind the compound's name is the strain that impose on TBBL. + is used to express the tensile strain.

Comp.	μ^*	$\omega_{\log}$	λ	T_c	Ref.
χ_3-B	0.1	323.43	0.95	24.7	[54]
β_{12}-B	0.1	384.16	0.89	18.7	[54]
tetr-Mo_2B_2	0.1	344.84	0.45	3.9	[55]
tri-Mo_2B_2	0.1	295.00	0.30	0.2	[55]
Cu_2Si	0.1	83.59	0.81	4.03	[29]
AlB_6	0.05	83.59	0.81	4.03	[23]
TiB_4 monolayer	0.1(0.05)	57.61	0.65	1.66(2.50)	This paper
TiB_4 bilayer	0.1(0.05)	459.12	0.35	0.82(2.98)	This paper
TiB_4 bilayer (+11%)	0.1(0.05)	223.47	0.65	6.43(9.66)	This paper

phonon spectrum of the seven strained structures with a strain in the range between 0% and 11%. These results indicate that the TBBL can exist at a tensile strain of 0–11%. The electronic band structures of the TBBL with the tensile strains of 0–11% are complied in Fig. 8. We find that the tensile strain of 0–11% does not change the existence of the nodal-line characteristic of the TBBL. Therefore, we investigated the EPC constant and the superconductivity of the TBBL with a tensile strain of 11% (Fig. 6). As compared with the strain-free case (0% tensile strain), the highest frequency is obviously reduced to 668 cm^{-1} and the EPC constant and T_c are however increased to 0.65 and 6.43 K (9.66 K, $\mu^* = 0.05$), which is higher than the boiling point of liquid helium (4.2 K).

D. Thermal stability

For practical applications, it is crucial to evaluate the thermal stability of 2D materials at elevated temperatures. In Ref. [30], the TBML was theoretically estimated to be able to stabilize up to a very high temperature of 2500 K. This fact implies that the TBML owns its outstanding thermal

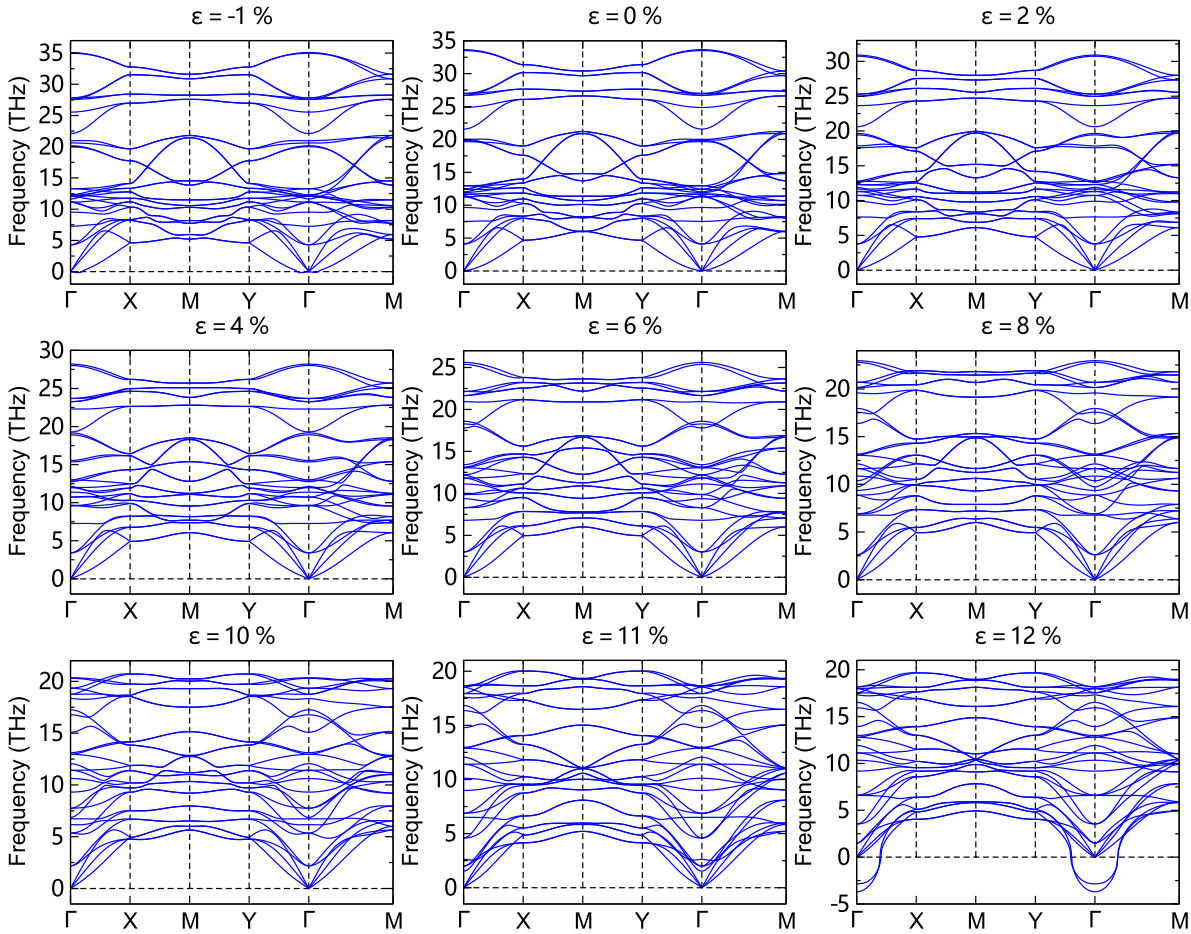

FIG. 7. The phonon dispersion relationships of TBBL with strain from –1% to 12%. The TBBL with strain –1% and 12% are dynamically unstable.

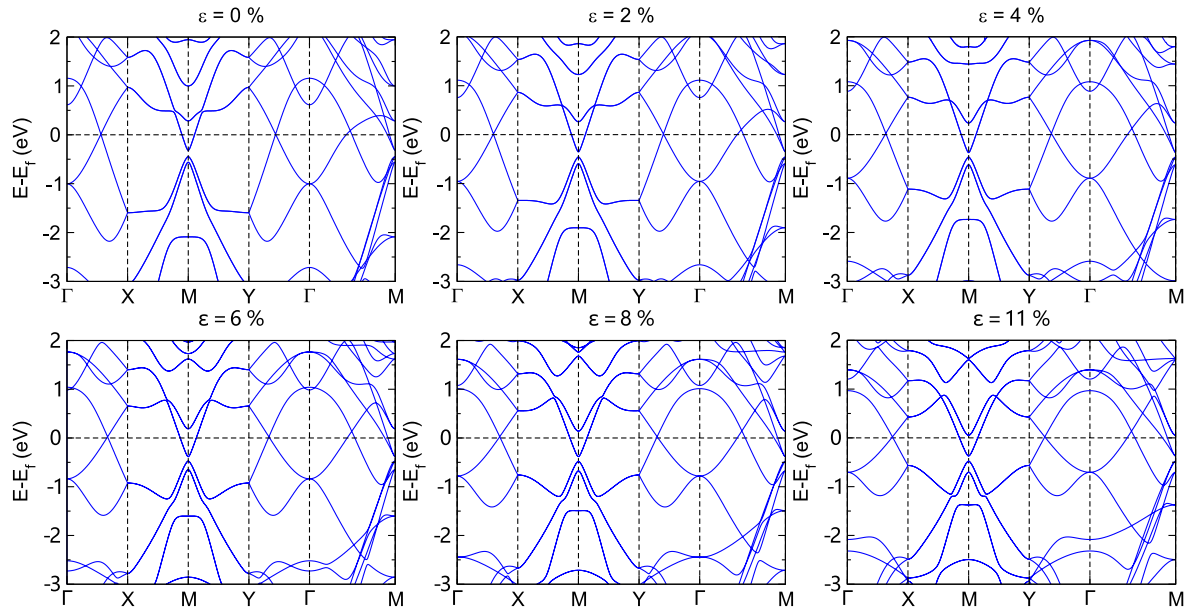

FIG. 8. The electronic band structures of the TBBL with strain ranging from 0%–11%.

stability. Next, we focused on the thermal stability of the TBBL. In order to simulate the thermal stability of the TBBL, we performed *ab initio* molecular dynamics (AIMD) simulations with a 3 × 3 × 1 TBBL supercell at different temperatures of 500, 1000, 1500, 2000, 2500, and 3000 K with a time length of 10 ps. The structures obtained from 10 ps simulated annealing at each temperature are shown in Fig. 9. The boron atoms in both the upper layer and lower layer maintain irregular 4+8 membered boron rings and the Ti atoms in both upper layer and lower layer almost remain a square-like shape until the temperature reaches 2500 K. When the temperature increases further to 3000 K, we found that the TBBL becomes unstable (see Fig. 9). This theoretical finding is similar to the TBML [30], revealing that the TBBL exhibits the excellent thermal stability as well. The high thermal stability will enable the TBBL to be applied to in both energy storage and Li-ion batteries anodes.

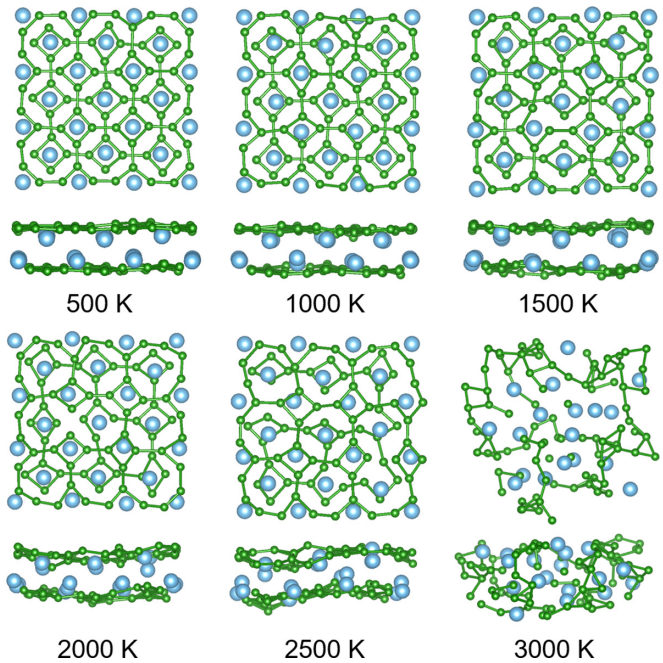

FIG. 9. Snapshots of the final frame of each *ab initio* molecular dynamics simulation from 500 to 3000 K (top and side views) after 10 ps of simulated annealing. Only those bonds within the simulated supercell are shown.

IV. CONCLUSIONS

In summary, by means of the first-principles calculations, we have investigated the electronic properties, lattice dynamics, EPC constant, and superconductivity of both TBML and TBBL. The results reveal that both the TBML and TBBL are topological nodal-line semimetals, which can be ascribed to the electronic band inversion between $B_{p_x+p_y}$ and B_{p_z} for the TBML and between $Ti_{d_{xz}+d_{yz}}$ and $Ti_{d_{z^2}}$ for the TBBL. Moreover, the nodal ring of the TBML is located around the *M* point, while the nodal ring of the TBBL is around the Γ point. The TBML possesses a higher EPC constant $\lambda = 0.65$, which is mainly contributed by the low-frequency out-of-plane phonon modes. Both the TBML and TBBL are phonon-mediated 2D superconductor with $T_c = 1.66$ K and 0.82 K, respectively. The T_c of TBBL can be increased to 6.43 K by imposing a tensile strain of 11% on the TBBL. Both TBML and TBBL can stabilize up to very high temperature of 2500 K.

ACKNOWLEDGMENTS

We thank Dr. Peitao Liu for proofreading the manuscript. Work was supported by the National Science Fund for Distinguished Young Scholars (Grant No. 51725103), by the National Natural Science Foundation of China (Grants No.

51671193 and No. 52001308). All calculations have been performed on the high-performance computational cluster in the Shenyang National University Science and Technology Park.

[1] J. Ishizuka, S. Sumita, A. Daido, and Y. Yanase, Phys. Rev. Lett. **123**, 217001 (2019).
[2] M. Sato and Y. Ando, Rep. Prog. Phys. **80**, 076501 (2017).
[3] S. D. Sarma, M. Freedman, and C. Nayak, npj Quantum Inf. **1**, 15001 (2015).
[4] X.-L. Qi and S.-C. Zhang, Rev. Mod. Phys. **83**, 1057 (2011).
[5] Z. Wang, Y. Sun, X.-Q. Chen, C. Franchini, G. Xu, H. Weng, X. Dai, and Z. Fang, Phys. Rev. B **85**, 195320 (2012).
[6] R. Li, H. Ma, X. Cheng, S. Wang, D. Li, Z. Zhang, Y. Li, and X.-Q. Chen, Phys. Rev. Lett. **117**, 096401 (2016).
[7] N. P. Armitage, E. J. Mele, and A. Vishwanath, Rev. Mod. Phys. **90**, 015001 (2018).
[8] J. Wang, Natl. Sci. Rev. **6**, 199 (2019).
[9] B. Albert and K. Hofmann, *in Handbook of Solid State Chemistry*, edited by R. Dronskowski, S. Kikkawa, and A. Stein (Wiley Online Library, New York, 2017), p. 435.
[10] N. Greenwood, R. Parish, and P. Thornton, Q. Rev. Chem. Soc. **20**, 441 (1966).
[11] H. Park, A. Encinas, J. P. Scheifers, Y. Zhang, and B. P. T. Fokwa, Angew. Chem., Int. Ed. **56**, 5575 (2017).
[12] J. Nagamatsu, N. Nakagawa, T. Muranaka, Y. Zenitani, and J. Akimitsu, Nature (London) **410**, 63 (2001).
[13] C. H. L. Kennard and L. Davis, J. Solid State Chem. **47**, 103 (1983).
[14] H. Niu, J. Wang, X.-Q. Chen, D. Li, Y. Li, P. Lazar, R. Podloucky, and A. N. Kolmogorov, Phys. Rev. B **85**, 144116 (2012).
[15] A. Knappschneider, C. Litterscheid, D. Dzivenko, J. A. Kurzman, R. Seshadri, N. Wagner, J. Beck, R. Riedel, and B. Albert, Inorg. Chem. **52**, 540 (2013).
[16] X.-Y. Cheng, X.-Q. Chen, D.-Z. Li, and Y.-Y. Li, Acta Crystallogr. C **70**, 85 (2014).
[17] X. Feng, C. Yue, Z. Song, Q. S. Wu, and B. Wen, Phys. Rev. Materials **2**, 014202 (2018).
[18] R. Lou, P. Guo, M. Li, Q. Wang, Z. Liu, S. Sun, C. Li, X. Wu, Z. Wang, Z. Sun *et al.*, npj Quantum Mater. **3**, 1 (2018).
[19] K.-H. Jin, H. Huang, J.-W. Mei, Z. Liu, L.-K. Lim, and F. Liu, npj Comput. Mater. **5**, 57 (2019).
[20] C. Buzea and T. Yamashita, Supercond. Sci. Technol. **14**, R115 (2001).
[21] A. Y. Liu, I. I. Mazin, and J. Kortus, Phys. Rev. Lett. **87**, 087005 (2001).
[22] R. Heid, B. Renker, H. Schober, P. Adelmann, D. Ernst, and K.-P. Bohnen, Phys. Rev. B **67**, 180510(R) (2003).
[23] B. Song, Y. Zhou, H.-M. Yang, J.-H. Liao, L.-M. Yang, X.-B. Yang, and E. Ganz, J. Am. Chem. Soc. **141**, 3630 (2019).
[24] H. Wang, C. Pan, S.-Y. Wang, H. Jiang, Y.-C. Zhao, Y.-H. Su, G.-H. Zhong, and C. Zhang, Int. J. Mod. Phys. C **32**, 2150057 (2020).
[25] D. Campi, S. Kumari, and N. Marzari, Nano Lett. **21**, 3435 (2021).
[26] A. Kononov, G. Abulizi, K. Qu, J. Yan, D. Mandrus, K. Watanabe, T. Taniguchi, and C. Schnenberger, Nano Lett. **20**, 4228 (2020).
[27] A. Kononov, M. Endres, G. Abulizi, K. Qu, J. Yan, D. G. Mandrus, K. Watanabe, T. Taniguchi, and C. Schnenberger, J. Appl. Phys. **129**, 113903 (2021).
[28] C. Liu, C. Chen, X. Liu, Z. Wang, Y. Liu, S. Ye, Z. Wang, J. Hu, and J. Wang, Sci. Adv. **6**, eaax7547 (2020).
[29] L. Yan, P.-F. Liu, T. Bo, J. Zhang, M.-H. Tang, Y.-G. Xiao, and B.-T. Wang, J. Mater. Chem. C **7**, 10926 (2019).
[30] X. Qu, J. Yang, Y. Wang, J. Lv, Z. Chen, and Y. Ma, Nanoscale **9**, 17983 (2017).
[31] Y. Wang, J. Lv, L. Zhu, and Y. Ma, Phys. Rev. B **82**, 094116 (2010).
[32] Z. Liu, E. Wu, J. Li, and S. Liu, Phys. Chem. Chem. Phys. **21**, 13151 (2019).
[33] G. Kresse and J. Furthmüller, Comput. Mater. Sci. **6**, 15 (1996).
[34] G. Kresse and J. Furthmüller, Phys. Rev. B **54**, 11169 (1996).
[35] G. Kresse and D. Joubert, Phys. Rev. B **59**, 1758 (1999).
[36] J. P. Perdew, K. Burke, and M. Ernzerhof, Phys. Rev. Lett. **77**, 3865 (1996).
[37] J. P. Perdew and A. Zunger, Phys. Rev. B **23**, 5048 (1981).
[38] P. Giannozzi, S. Baroni, N. Bonini, M. Calandra, R. Car, C. Cavazzoni, D. Ceresoli, G. L. Chiarotti, M. Cococcioni, I. Dabo *et al.*, J. Phys.: Condens. Matter **21**, 395502 (2009).
[39] P. Giannozzi, O. Andreussi, T. Brumme, O. Bunau, M. B. Nardelli, M. Calandra, R. Car, C. Cavazzoni, D. Ceresoli, M. Cococcioni *et al.*, J. Phys.: Condens. Matter **29**, 465901 (2017).
[40] N. Marzari, D. Vanderbilt, A. De Vita, and M. C. Payne, Phys. Rev. Lett. **82**, 3296 (1999).
[41] S. Baroni, S. de Gironcoli, A. Dal Corso, and P. Giannozzi, Rev. Mod. Phys. **73**, 515 (2001).
[42] A. A. Mostofi, J. R. Yates, G. Pizzi, Y.-S. Lee, I. Souza, D. Vanderbilt, and N. Marzari, Comput. Phys. Commun. **185**, 2309 (2014).
[43] Q. Wu, S. Zhang, H.-F. Song, M. Troyer, and A. A. Soluyanov, Comput. Phys. Commun. **224**, 405 (2018).
[44] J. Li, L. Wang, J. Liu, R. Li, Z. Zhang, and X.-Q. Chen, Phys. Rev. B **101**, 081403(R) (2020).
[45] Y. Kim, B. J. Wieder, C. L. Kane, and A. M. Rappe, Phys. Rev. Lett. **115**, 036806 (2015).
[46] J.-L. Lu, W. Luo, X.-Y. Li, S.-Q. Yang, J.-X. Cao, X.-G. Gong, and H.-J. Xiang, Chin. Phys. Lett. **34**, 057302 (2017).
[47] D. Shao, T. Chen, Q. Gu, Z. Guo, P. Lu, J. Sun, L. Sheng, and D. Xing, Sci. Rep. **8**, 1467 (2018).
[48] A. Molina-Sánchez and L. Wirtz, Phys. Rev. B **84**, 155413 (2011).
[49] J.-A. Yan, W. Y. Ruan, and M. Y. Chou, Phys. Rev. B **77**, 125401 (2008).
[50] E. S. Penev, A. Kutana, and B. I. Yakobson, Nano Lett. **16**, 2522 (2016).
[51] J. Dai, Z. Li, J. Yang, and J. Hou, Nanoscale **4**, 3032 (2012).
[52] A. Leonardo, I. Y. Sklyadneva, V. M. Silkin, P. M. Echenique, and E. V. Chulkov, Phys. Rev. B **76**, 035404 (2007).
[53] J.-A. Yan, R. Stein, D. M. Schaefer, X.-Q. Wang, and M. Y. Chou, Phys. Rev. B **88**, 121403(R) (2013).

[54] M. Gao, Q.-Z. Li, X.-W. Yan, and J. Wang, Phys. Rev. B **95**, 024505 (2017).
[55] L. Yan, T. Bo, P.-F. Liu, B.-T. Wang, Y.-G. Xiao, and M.-H. Tang, J. Mater. Chem. C **7**, 2589 (2019).
[56] D.-L. Nguyen, C.-R. Hsing, and C.-M. Wei, Nanoscale **11**, 17052 (2019).
[57] E. Navarro-Moratalla, J. O. Island, S. Mañas Valero, E. Pinilla-Cienfuegos, A. Castellanos-Gomez, J. Quereda, G. Rubio-Bollinger, L. Chirolli, J. A. Silva-Guillén, N. Agraït *et al.*, Nat. Commun. **7**, 2041 (2016).
[58] P. B. Allen and R. C. Dynes, Phys. Rev. B **12**, 905 (1975).
[59] S. Ichinokura, K. Sugawara, A. Takayama, T. Takahashi, and S. Hasegawa, ACS Nano **10**, 2761 (2016).
[60] E. R. Margine, H. Lambert, and F. Giustino, Sci. Rep. **6**, 21414 (2016).
[61] L. Wang, Y. Shi, M. Liu, A. Zhang, Y.-L. Hong, R. Li, Q. Gao, M. Chen, W. Ren, H.-M. Cheng, Y. Li, and X.-Q. Chen, Nat. Commun. **12**, 2361 (2021).
[62] S.-L. Yang, J. A. Sobota, C. A. Howard, C. J. Pickard, M. Hashimoto, D. H. Lu, S.-K. Mo, P. S. Kirchmann, and Z.-X. Shen, Nat. Commun. **5**, 3493 (2014).
[63] C. Si, Z. Liu, W. Duan, and F. Liu, Phys. Rev. Lett. **111**, 196802 (2013).
[64] D. F. Shao, W. J. Lu, H. Y. Lv, and Y. P. Sun, Europhys. Lett. **108**, 67004 (2014).